ADVANCED FUNCTIONAL MATERIALS
www.afm-journal.de

An Efficient Fiber Gel Dye-Sensitized Solar Cell with Stable Interlaced Interfaces

Xinyue Kang, Jiatian Song, Jiuzhou Liu, Siwei Cao, Zhengmeng Lin, Hongyu Jiang, Yiqing Yang, Xiangran Cheng, Yulu Ai, Xuemei Sun, Kaiwen Zeng, Zhengfeng Zhu, and Huisheng Peng**

Fiber gel dye-sensitized solar cells (FGDSCs) are recognized as an effective solution for high-performance, durable and safe wearable power supply. However, poor and unstable interfaces between fiber electrodes and gel electrolytes are bottleneck problems that have restricted the photovoltaic performances of FGDSCs and their stabilities during deformations. Here, an FGDSC with stable interlaced interfaces is designed by incorporating polymerized gel electrolyte into the aligned channels in fiber electrodes and the gaps between photoanode and counter electrode in situ. The interlaced structure of gel electrolyte in FGDSC improves the interfacial stability and provided stable channels for rapid ion diffusions, offering efficient charge transports at interfaces. The resulting FGDSC thus produced a high power conversion efficiency of 7.95%, and it is further maintained by over 90% after bending for 5000 cycles. These FGDSCs can be integrated with fiber batteries as a self-charging power system, demonstrating an effective power solution for wearables.

1. Introduction

In recent years, wearable technology has been widely explored for many important fields such as sports monitoring, medical health, and communication, and is expected to enhance interactivity and diversity to promote intelligent life for human beings.[1–4] However, the increasing conflicts between the growing power consumption of wearables and the low capacity of built-in batteries have proposed urgent demands on the effectivity, durability, and even sustainability of wearable power supplies.[5–7] To this end, flexible fiber solar cells, as efficient real-time power conversion devices, are expected to meet the requirements for high flexibility and durability of wearable power modules.[8–11] Fiber dye-sensitized solar cells with merits of easy preparation, low cost, and high performance have attracted wide attention,[12–16] in which fiber gel dye-sensitized solar cells (FGDSCs) that can avoid electrolyte leakage are promising alternatives because their high safety in wearable applications.[17–19]

Unfortunately, due to the natural difficulties in constructing high-quality films on curved fibers and establishing stable interfaces between functional layers, current FGDSCs usually showed poor interfaces, especially between irregular fiber electrodes and gel electrolytes.[20–23] As a result, the incompact contacts between the counter electrode and electrolyte greatly hindered efficient reactions of redox mediators at interfaces for charge transports, causing severe charge recombination. Meanwhile, the weak and unstable interfaces in FGDSCs would be easily destroyed under deformations, further deteriorating their photovoltaic performances.[24] Therefore, the serious interfacial issues in present FGDSCs resulted in low power conversion efficiencies (PCEs) and poor mechanical stabilities, which have restricted their further developments and real applications in wearables. Despite the urgent demands, efficient and stable FGDSCs are unavailable yet.

In this work, we designed an FGDSC with the incorporation of polymerized gel electrolyte into the aligned channels in fiber electrodes and the gaps between photoanode and counter electrode in situ. In the FGDSC, the photoanode was composed of TiO_2 nanotube arrays grown on a Ti wire, while the counter electrode was made from a bunch of primary carbon nanotube (CNT) fibers twisted together, showing aligned micrometer-scale channels. CNT fibers are good candidates for counter electrodes due to their promising advantages of low cost, high conductivity, mechanical flexibility, and large specific surface areas.[25–28] The polyurethane (PU)-based gel electrolyte with high mechanical properties was formed on the irregular surfaces of fiber electrodes and even in their internal channels by in situ polymerization, realizing compact and stable interlaced interfaces between fiber electrodes and electrolytes. The interlaced structure produced stable channels for rapid ion diffusions and tight interfaces promoted efficient interfacial charge transports, beneficial to reduce charge recombination. The resulting FGDSC presented a

X. Kang, J. Song, J. Liu, S. Cao, Z. Lin, H. Jiang, Y. Yang, X. Cheng, Y. Ai, X. Sun, K. Zeng, Z. Zhu, H. Peng
State Key Laboratory of Molecular Engineering of Polymers
Department of Macromolecular Science
and Institute of Fiber Materials and Devices
Fudan University
Shanghai 200438, China
E-mail: zhuzf@fudan.edu.cn; penghs@fudan.edu.cn

The ORCID identification number(s) for the author(s) of this article can be found under https://doi.org/10.1002/adfm.202404361

DOI: 10.1002/adfm.202404361

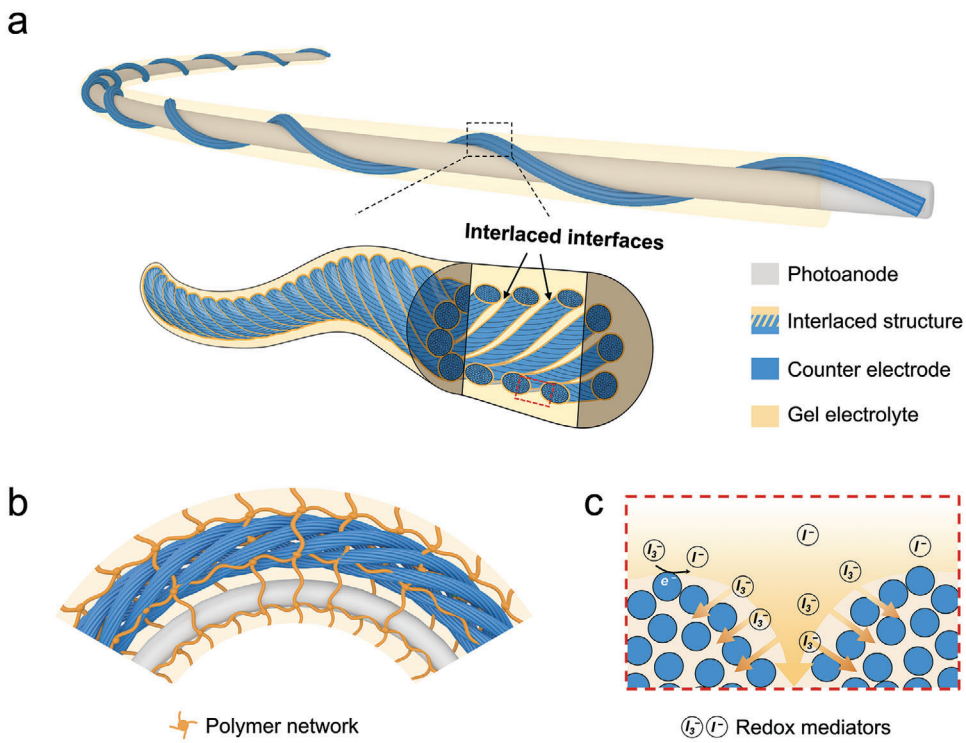

Figure 1. Schematic diagram of FGDSC with interlaced interfaces. a) Diagram illustrating the device structure of FGDSC with a photoanode, a counter electrode with aligned channels, and a gel electrolyte filling the gap between two electrodes. The enlarged diagram shows the interlaced interfaces between the gel electrolyte and the counter electrode. b) Schematics of the FGDSC with penetrative polymer networks connecting the two electrodes under flexure. c) Diagram illustrating that the interlaced interfaces provide channels for rapid diffusion and reaction of redox mediators.

high PCE of 7.95%, and it could be maintained by over 90% after bending for 5000 cycles, demonstrating high mechanical stability. These FGDSCs were further integrated with fiber batteries into textiles as power supply systems, demonstrating broad application prospects in the wearable field.

2. Results and Discussion

Figure 1a depicts the schematic structure of the designed FGDSC, displaying that a fiber counter electrode with aligned channels was twisted around a photoanode and fully covered with gel electrolyte. The gel electrolyte was obtained by in situ polymerization from low-viscosity electrolyte precursors, which had been sufficiently infiltrated into irregular surfaces and inner channels of fiber electrodes, resulting in interlaced interfaces. The formed elastic gel networks connected two electrodes tightly, improving their interfacial stability even during drastic deformations (Figure 1b). Moreover, the interlaced structure with compact interfaces also established stable channels for rapid ion diffusions, offering efficient transports and collections of interfacial charges (Figure 1c).

The FGDSC can be fabricated as schematically illustrated in **Figure** 2a. In brief, a fiber counter electrode was twisted around a fiber photoanode and then encapsulated into a transparent tube. The gel electrolyte precursor solution was injected into the tube and polymerized in situ to produce an FGDSC (Figure 2b,c). Here, the photoanode was composed of aligned TiO_2 nanotube arrays synthesized on a Ti wire by anodization (Figure 2d). The counter electrode was made from a bunch of primary carbon nanotube (CNT) fibers twisted together, showing aligned micrometer-scale channels (Figure 2e). The primary CNT fibers were obtained by the floating catalyst vapor deposition method[29–31] (Figure S1, Supporting Information), and their diameters were regulated by the feeding and winding rates. Then, the average sizes of aligned channels from 0.6 to 2.3 μm were effectively realized by synergistically controlling the diameters and quantities of primary CNT fibers (Figure S2, Supporting Information).

The gel precursor solution made from a 3-methoxypropionitrile-based liquid electrolyte incorporated with poly(ethylene adipate), isophorone diisocyanate, and hexamethylene diisocyanate trimer showed a low viscosity of ≈9 mPa s (Figure S3, Supporting Information), which can easily infiltrate into irregular surfaces of fiber electrodes. The photoanode consisting with aligned TiO_2 nanotubes also showed "V-type" channels due to their geometrical structure, which facilitated the infiltration of the electrolyte precursor solution. Meanwhile, the constructed aligned channels in the counter electrode would further facilitate rapid and deep infiltration of precursor solution in contrast with dense CNT fibers typically used as counter electrodes (Figure S4, Supporting Information). After in situ polymerization, the gel electrolyte and counter electrode formed a stable interlaced structure through the internal channels and established compact interfaces between electrolyte and fiber electrodes (Figure 2f,g). Figure S5 (Supporting Information) presents additional SEM images to identify channels

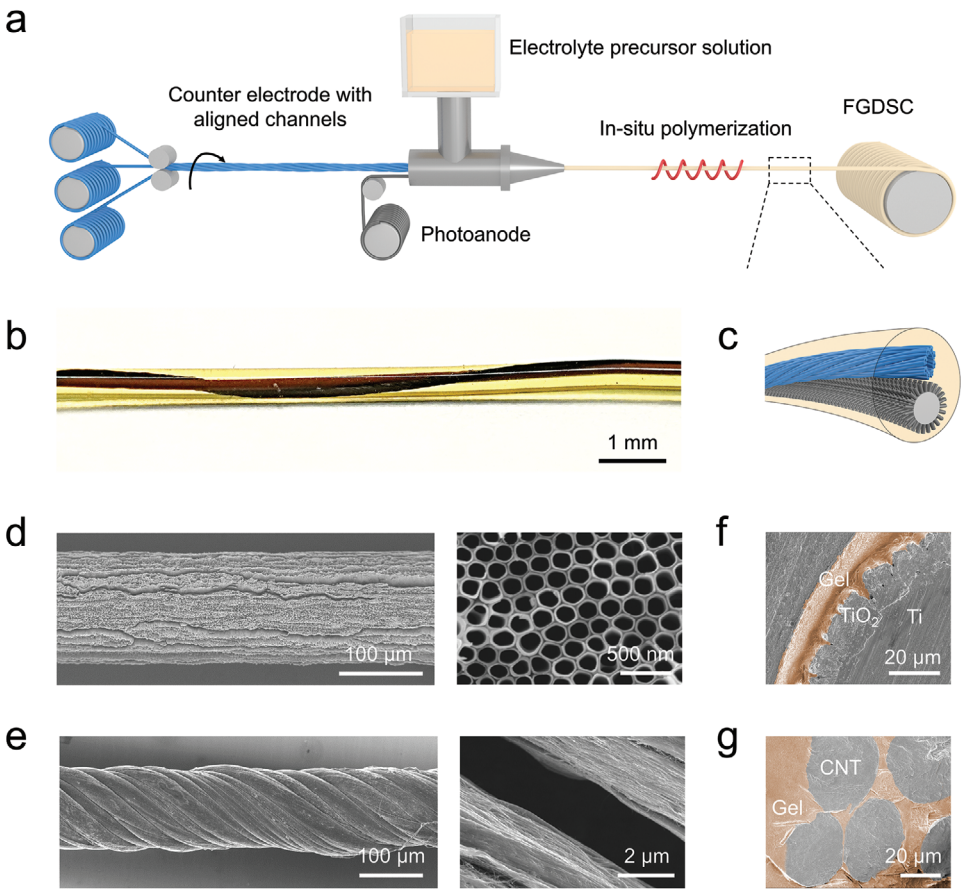

Figure 2. Fabrication and structure of the designed FGDSC with interlaced interfaces. a) Diagram illustrating the fabrication flow of the FGDSC. A bunch of CNT fiber was twisted together to achieve a counter electrode with aligned channels. The counter electrode was then twisted around a fiber photoanode encapsulated into a tube injected with electrolyte precursor solution. After in situ polymerization, the FGDSC was obtained. b) Photograph of the prepared FGDSC. c) Sketch map of the enlarged structure of the FGDSC. d) Scanning electron microscopy (SEM) image of the photoanode with TiO_2 nanotube arrays growing on a Ti wire at low and high resolutions. e) SEM image of the counter electrode with aligned channels in CNT fiber at low and high resolutions. f,g) Cross-sectional SEM images of the photoanode and counter electrode embedded with the gel electrolyte, respectively. To identify the fiber electrodes and gel electrolyte for convenience, an orange layer was added to the region of gel electrolyte.

and infused gel electrolytes between primary CNT fibers. Compared to in situ polymerization method, it was difficult to form compact interfaces on irregular fiber surfaces through directly coating preheated gel electrolytes, such as the widely used poly(vinylidene fluoride-co-hexafluoropropylene) [P(VDF-HFP)]-based electrolyte[32,33] with a high viscosity over 1400 mPa s, which can neither infiltrate into CNT fibers nor adhere tightly to their surfaces (Figure S6, Supporting Information).

Figure 3a–c schematically illustrates typical interfacial structures between gel electrolyte and CNT fiber, including the incompact interfaces and the compact interfaces without and with interlaced structures, respectively. The incompact interfaces were between CNT fiber and coated P(VDF-HFP)-based gel electrolyte, and the compact interfaces without and with interlaced structure were formed by in situ polymerized PU-based gel electrolyte on CNT fibers without and with aligned channels, respectively. We first investigated the mechanical stability of interfaces between gel electrolyte and counter electrode. The resistances between CNT fiber and coated P(VDF-HFP)-based gel electrolyte were dramatically increased by 99% after bending for 5000 cycles due to incompact interfaces, while the resistances between CNT fiber and in situ polymerized PU gel electrolyte showed a lower increase of ≈23% (Figure 3d). The improved stability was attributed to the tight connections formed by in situ polymerization and the inherently high mechanical properties of PU[34] like good stretchability and resilience (Figure S7a,b, Supporting Information), which would effectively release interfacial stresses even during complex deformations. On the contrary, P(VDF-HFP)-based gel usually exhibited worse deformability (Figure S7c, Supporting Information).[35] Moreover, the interlaced structure further enhanced interfacial stabilities, reflected by the much lower variation of less than 8% in interfacial resistances (Figure 3d). This may originate from the enhanced interfacial adhesion strength (up to 135.9 kPa) after designing interlaced structure, which was two times higher than those without interlaced interfaces (Figure 3e), while the adhesion strength of incompact interfaces even could not be measured owing to extreme brittleness of P(VDF-HFP)-based gel. Therefore, the separation of interfaces was effectively prevented during deformations (Figure S8, Supporting Information), resulting in stable

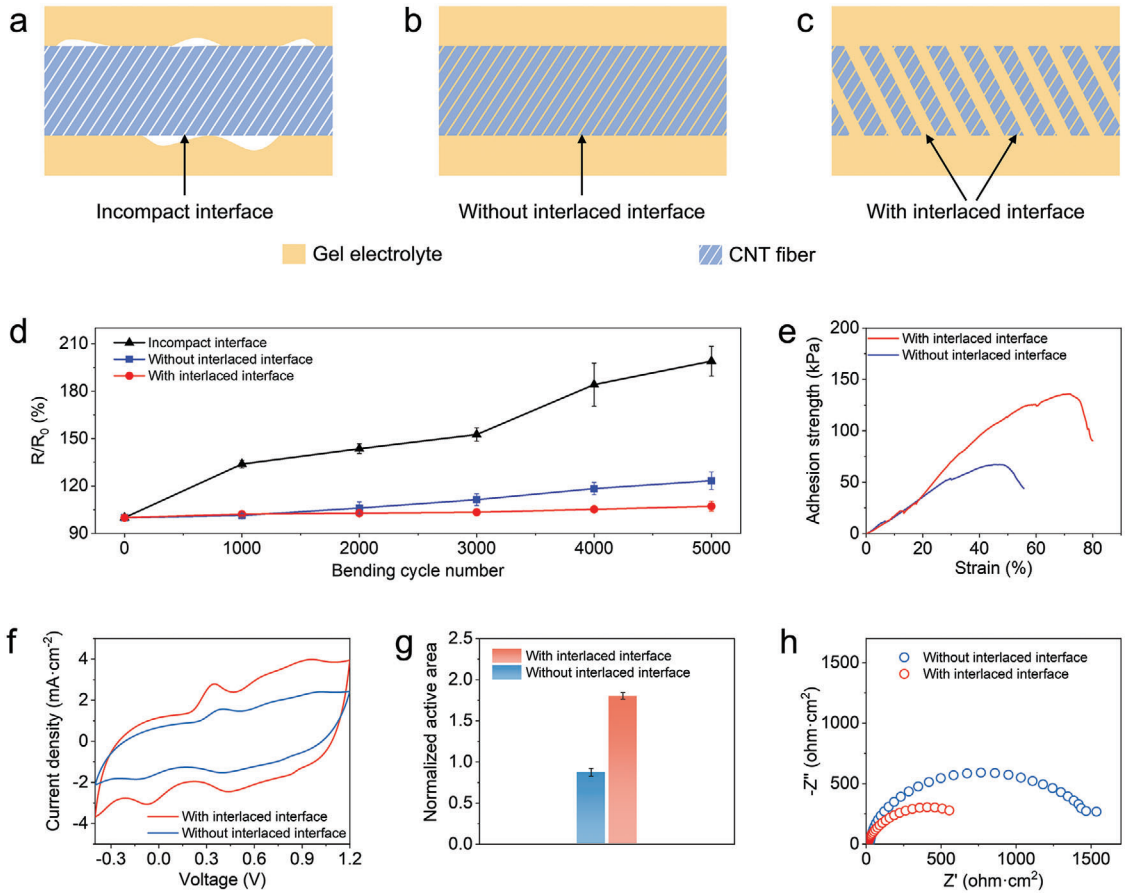

Figure 3. Properties of the designed interfaces with interlaced structure. a–c) Schematically illustrating typical interfacial structures including the incompact interfaces and the compact interfaces without and with interlaced structure, respectively. The incompact interfaces were between CNT fiber and coated P(VDF-HFP)-based gel electrolyte, and the compact interfaces without and with interlaced structure were formed by in situ polymerized PU-based gel electrolyte on CNT fibers without and with aligned channels, respectively. d) Variation of interfacial resistances between counter electrode and gel electrolyte during bending for 5000 cycles (curvature radius of 1 cm). R_0 and R correspond to the resistances before and after bending, respectively. Error bars show standard deviations for the results from three samples. e) Adhesion strength of interfaces between counter electrode and gel electrolyte with and without interlaced structure. f) Cyclic voltammogram curves of the counter electrodes with and without interlaced interfaces, showing reduction peak current densities of −3.064 mA cm^{-2} at −0.075 V, and −1.847 mA cm^{-2} at −0.144 V, and peak-to-peak voltage separations of 0.422 and 0.549 V, respectively. g) The normalized active areas of the counter electrodes with and without interlaced interfaces were 1.80 ± 0.04 and 0.88 ± 0.05, respectively. Error bars show standard deviations for the results from three samples. h) Nyquist plots of symmetrical cells with two identical electrodes measured at 0 V from 100 kHz to 0.01 Hz. The Nernst diffusion impedances of the counter electrodes with and without interlaced interfaces were 787.5 and 1475.2 Ω cm^2, respectively. The charge transfer resistances of the counter electrode with and without interlaced interfaces were 2.08 and 550.82 Ω cm^2, respectively.

electronic properties. That is, the construction of interlaced structures with intimate and stable interfaces between fiber electrodes and gel electrolytes was conducive to improving the mechanical and electrical stabilities of FGDSCs.

We further investigated the electrochemical properties of CNT fibers in gel electrolytes. The PU-based gel electrolyte showed a conductivity of 7.31 mS cm^{-1} close to 7.92 mS cm^{-1} of P(VDF-HFP)-based electrolyte (Figure S9a, Supporting Information). Benefitted from the improved infiltration and intimate interfaces formed by in situ polymerization, the CNT fiber incorporated with PU-based electrolyte exhibited enhanced electrocatalytic activities toward I^-/I_3^- redox reaction by cyclic voltammetry in Figure S9b (Supporting Information). Furthermore, the counter electrode with interlaced structure showed higher electrocatalytic activity, verified by the higher reduction peak current density of −3.064 mA cm^{-2} at −0.075 V and narrower peak-to-peak voltage separation of 0.422 V between the oxidation and reduction peaks (Figure 3f). This may be attributed to remarkably increased electrochemical active areas (Figure 3g), and the interlaced structure exposed large amounts of active sites for efficient redox reactions.

Subsequently, we used two symmetrical electrodes to assemble the dummy cells and characterized their ion diffusion properties by electrochemical impedance spectroscopy (Figure 3h). The equivalent circuit for fitting impedance spectroscopy is given in Figure S10 (Supporting Information). The cells made from the dense CNT fibers combined with in situ polymerized gel electrolyte exhibited high Nernst diffusion impedance (Z_N), reflecting low diffusion rates of ions in gel electrolytes. In contrast, the cells with the design of interlaced interfaces between fiber electrodes and electrolytes showed much lower Z_N, indicating

that this structure established stable channels for rapid ion diffusions in counter electrodes and shortened ion transport pathways, which was beneficial to reduce charge recombination. Electrochemical impedance spectroscopy in Figure 3h can also characterize charge transfer resistance (R_{CT}) represented by the semicircle at high frequency to investigate interfacial charge transfer kinetics. The R_{CT} of the counter electrode with interlaced interfaces was 2.08 Ω cm^2, much lower than that of the counter electrode without interlaced interfaces (550.82 Ω cm^2). We further characterized the Tafel polarization curves, as shown in Figure S11 (Supporting Information). The extrapolated intercept of the left branch at the Tafel zone identifies the exchange current density which is inversely related to R_{CT}.[27,36] The counter electrode with interlaced interfaces exhibited an improved exchange current density, confirming its advantage in interfacial charge transfer kinetics, which can be attributed to its higher electrochemical active areas (Figure 3g). The counter electrodes composed of more primary CNT fibers can provide more channels and enhance the electrochemical active areas, but too small channel sizes would also impend diffusions of redox couples, causing increased Z_N values (Figure S12a,b, Supporting Information). Therefore, the counter electrode with a channel size of 1.3 µm presented both large electrochemical active areas and low Z_N, presenting the optimal photovoltaic performances (Figure S12c and Table S1, Supporting Information).

Owing to the interlaced structure with compact interfaces that established stable channels for rapid ion diffusions and efficient interfacial charge transports, the charge recombination was greatly reduced, leading to a higher photocurrent.[37,38] The resulting FGDSC realized obviously improved photovoltaic performances, producing a high PCE of 7.95%, with open-circuit voltage (V_{OC}), short-circuit current density (J_{SC}), and fill factor (FF) of 0.75 V, 15.88 mA cm^{-2}, and 0.67, respectively (**Figure 4a**; Table S1, Supporting Information), which is the highest value of reported FGDSCs to date[32,39–54] (Figure 4b; Table S2, Supporting Information). The incident photo-to-electron conversion efficiency (IPCE) spectra of the FGDSC with interlaced interfaces showed higher IPCE values at the response range of 400–730 nm wavelengths than those of the FGDSC without interlaced interfaces (Figure S13, Supporting Information). The integrated current density of FGDSC with interlaced interfaces was increased by 26.2%, consistent with the increase in photocurrent (25.9%). The influences of the diameter and length of CNT fiber electrodes on the performances of FGDSCs were investigated (Figures S14 and S15, Supporting Information). The increase in electrode diameter caused higher PCEs of FGDSCs, indicating that the enhanced active area was the main factor affecting PCEs of FGDSCs. However, too thick counter electrodes may block photoanodes from receiving light, slightly lowering the PCE. Therefore, the optimal diameter of CNT fiber was 150 µm. Longer length of CNT fiber would increase the axial resistance, causing a PCE deterioration of the FGDSC, while this issue can be effectively alleviated by improving the conductivity of CNT fibers, such as the incorporation with metal current collectors.[1,13] Current density–voltage (J–V) curves of the FGDSC were measured in both forward and reverse directions, showing a normal hysteresis behavior (Figure S16, Supporting Information), which was considered the relation to the kinetics of accumulation of positive charges at the TiO_2 interfaces and the extent of surface recombination.[55] The PCEs from 30 FGDSCs showed a narrow distribution, indicating a highly repeatable fabrication process and stable photovoltaic performances of our FGDSCs (Figure 4c). This strategy of fabricating FGDSCs with interlaced interfaces can also be applied to other material systems containing the fiber electrodes with channel structure and the gel electrolyte that can be polymerized in situ. Certainly, the photovoltaic performances highly depend on the inherent material characteristics. For instance, the FGDSC using commercial carbon fiber as the counter electrode achieved a lower PCE of 4.56%, attributed to its smaller active area and lower conductivity compared with CNT fiber (Figure S17, Supporting Information).

Moreover, the fabricated FGDSCs can cope with a variety of complex deformations in wearable applications. Their PCEs had been maintained by over 90% after bending or twisting for 5000 cycles (Figure 4d). The FGDSCs could also effectively work at increasing temperatures from −20 °C to 60 °C and below atmospheric pressure (Figure 4e,f). The lower PCEs at low temperatures can be improved by designing thermal management systems to keep FGDSCs within an appropriate temperature range. Also, the FGDSCs showed high stability with their PCEs maintained by 92% for 10 days (Figure S18, Supporting Information). Furthermore, after the FGDSCs were cut off, no electrolyte was leaked, and they could also provide stable output voltage and successfully power a hygrothermograph (Figure 4g), demonstrating their high stability and safety in real applications.

The FGDSCs were further integrated with fiber batteries into textiles as a self-charging power supply system, in which energy harvesting modules can achieve desired output voltages and currents through the connections of FGDSCs in series and parallel (Figure S19, Supporting Information). The electricity converted by photovoltaic modules successfully charged a fiber lithium-ion battery from 3.0 to 4.4 V under simulated sunlight (Figure S20, Supporting Information). The charge rate was controlled by matching the output current of FGDSCs with the capacity of fiber lithium-ion battery (Figure S21, Supporting Information). The power system can be woven into daily clothing and supply power for various wearable devices, such as portable walkie-talkie and smart wristband (Figure 4h–j), providing an effective solution addressing the limited working duration of wearables.

3. Conclusion

In summary, we have constructed an FGDSC with compact and stable interlaced interfaces between gel electrolyte and fiber electrodes, realizing high mechanical stability and electrochemical properties. The resulting FGDSC showed the highest PCE of 7.95% and high durability under deformations. The FGDSCs were integrated with fiber batteries into textiles as power supply systems, which provided an effective power solution addressing the limited working duration of wearables and demonstrated potentials for future applications in smart electronic textiles.

4. Experimental Section

Materials: All materials, including titanium wire (metal basis: 99.9%, diameter: 127 µm, Alfa Aesar), ammonium fluoride (metal basis: 99.99%, Aladdin), ethylene glycol (99.5%, Sinopharm), tert-butyl alcohol (99%,

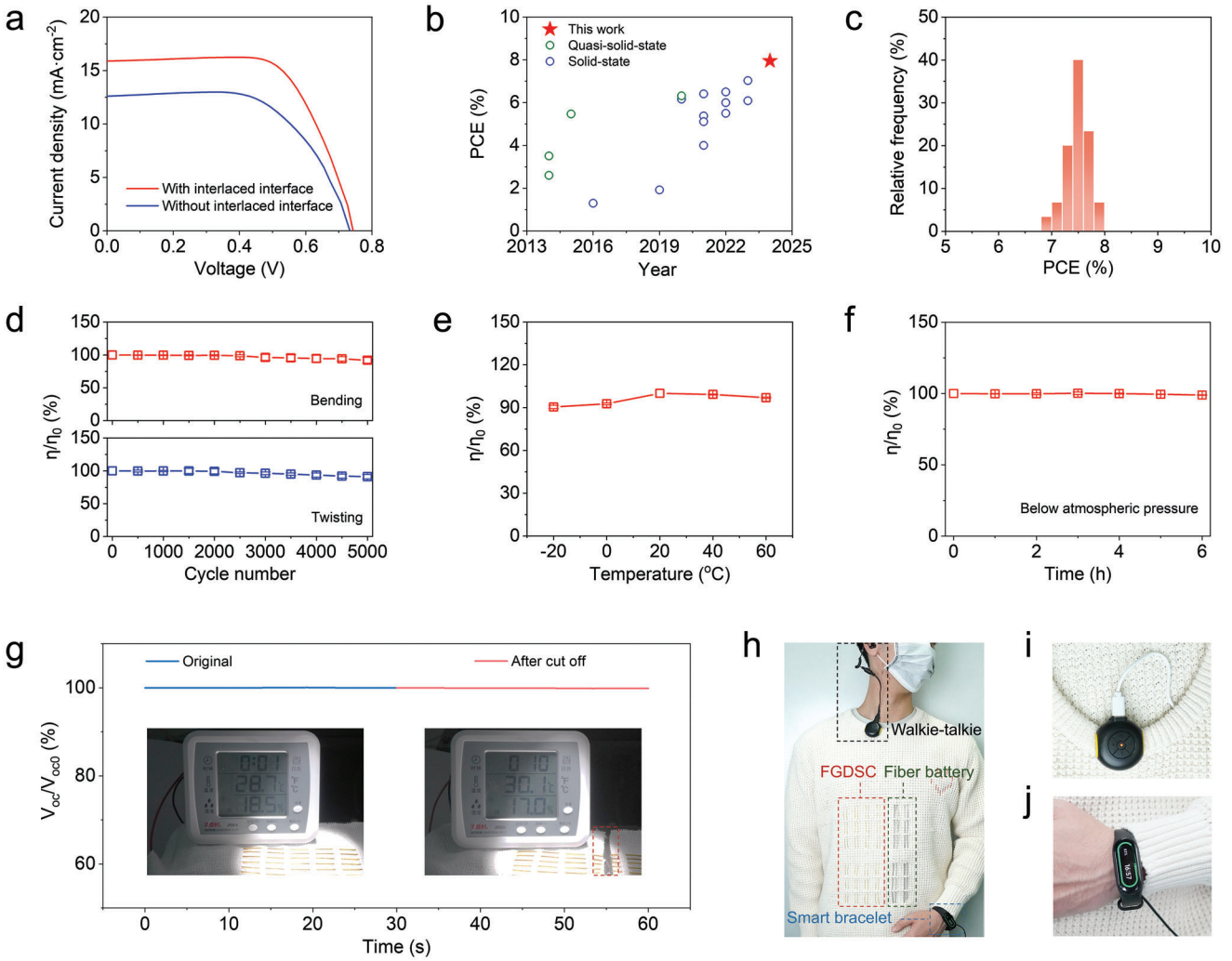

Figure 4. Properties of FGDSCs with interlaced interfaces. a) *J*–*V* curves of FGDSCs with and without interlaced interfaces. b) PCE of the resulting FGDSC in comparison to those of the reported quasi-solid-state[32,39–42] and solid-state[43–54] fiber dye-sensitized solar cells in previous studies. c) PCE statistics of 30 FGDSCs. d) Mechanical stability of FGDSCs against bending and twisting. The PCEs maintained over 90% after 5000 cycles for each deformation mode. e,f) Stability of FGDSCs under different temperatures and below atmospheric pressure. Their PCEs showed variations of less than 10% from −20 to 60 °C and the PCEs were varied below 2% at 20 kPa for 6 h. Error bars show standard deviations for the results from three samples in (d–f). g) Stability of the FGDSC after cutting off. The open-circuit voltage showed nearly no variation. Inset, photographs of FGDSCs powering a hygrothermograph before and after cutting off. h–j) Photograph of a daily clothing integrated with FGDSCs and fiber lithium-ion batteries charging a walkie-talkie and a smart bracelet.

Aladdin), acetonitrile (98%, Aladdin), N719 dye (HPLC: 90%, Yingkou OPV Tech New Energy Co., Ltd.), iodine (99.8%, J&K), lithium iodide (anhydrous, 98.5%, J&K), 1,2-dimethyl-3-propylimidazolium iodide (98%, TCI), 4-tert-butylpyridine (96%, Aladdin), 3-methoxypropionitrile (98%, Sinopharm), poly(ethylene adipate) (M_W~2000, Aladdin), isophorone diisocyanate (99%, Aladdin), ditin butyl dilaurate (95%, Aladdin), hexamethylene diisocyanate trimer (99%, MACKLIN), poly(vinylidene fluoride-co-hexafluoropropylene (pellets, Sigma-Aldrich), thiophene (99%, Aladdin), ferrocene (99%, Aladdin), ethanol (99.7%, Sinopharm), decahydronaphthalene (99%, Aladdin), $LiClO_4$ (99.9%, Aladdin), K_2PtCl_6 (99.9%, Aladdin), $K_4Fe(CN)_6$ (99.9%, Aladdin), KCl (99.9%, Aladdin), and transparent packaging tubes (inner diameter of 600 µm, outer diameter of 1000 µm, Zhongshan Wolida Electronic Material Co., Ltd.) were commercially available and used without further treatment unless otherwise mentioned.

Preparation of Counter Electrodes: CNT fibers were synthesized by floating catalyst chemical vapor deposition method. The feed solution contained ethanol as a carbon resource, 2.5 wt% ferrocene, and 2 wt% thiophene as composite catalyst. The solution was pumped into the furnace at a feeding rate of 1–6 mL h^{-1} and reacted at 1250 °C in H_2 and Ar atmosphere. The synthesized CNT aerogels were pulled out of the furnace, densified by water, and wound onto reels at a winding rate range of 150–300 m h^{-1} to form CNT fibers. The diameters of CNT fibers could be tuned by varying feeding and winding rates. In this work, the CNT fibers with diameters of 25, 45, and 65 µm were used as primary fibers. Then, a bunch of primary CNT fibers were twisted together by a rotating motor at a rotating speed of 200 rpm for 60 s to prepare counter electrodes (diameter of 150 µm) with aligned channels. The amounts of primary CNT fibers used were 30, 15, and 5, respectively. The average sizes of produced channels were 0.6, 1.3, and 2.3 µm, respectively.

Preparation of Fiber Photoanodes: Titanium wires were modified with titanium dioxide nanotube arrays via an anodic oxidation method in a glycol solution composed of 3.3 g L^{-1} NH_4F and 88 g L^{-1} H_2O at 60 V and 45 °C for 6 h. The Ti/TiO_2 wires were annealed at 500 °C for 60 min in a muffle furnace. The cooled Ti/TiO_2 wires were immersed in a dye solution containing 0.3 mM N719 dye in tert-butanol/acetonitrile (1/1, v/v) for 24 h.

Preparation of Electrolyte Precursor Solution: The liquid electrolyte was composed of 6 mM I_2, 0.1 M LiI, 0.6 M 1,2-dimethyl-3-propylimidazolium iodide, and 1 M 4-*tert*-butylpyridine in 3-methoxypropionitrile. The precursor solution was prepared by dissolving 12 wt% poly(ethylene adipate) in liquid electrolyte, followed by the addition of 0.3 wt% isophorone diisocyanate, 1.7 wt% hexamethylene diisocyanate trimer, and 0.1 wt% ditin butyl dilaurate. In particular, poly(ethylene adipate) needs to be dehydrated before use by heated to 120 °C under vacuum for 1 h.

Fabrication of FGDSCs: The counter electrode was twisted around the as-prepared photoanode with gaps inevitably generated between them due to their inherent cylindrical shapes. The gaps were maintained by knotting both ends of the counter electrode to the photoanode. Then two electrodes were inserted in a flexible transparent tube, followed by injection of the electrolyte precursor solution. Subsequently, they were heated at 45 °C for 6 h to form the FGDSC.

Fabrication of Fiber Lithium-ion Batteries: An aluminum wire coated with positive slurry (lithium cobalt oxide, super-P, polyvinylidene fluoride, and N-methyl-2-pyrrolidone) was used as fiber positive electrode (diameter of 200 µm). A copper wire coated with negative slurry (graphite, super-P, sodium carboxymethyl cellulose, butadiene styrene rubber, and water) was used as a fiber negative electrode (diameter of 200 µm). The negative electrodes were wrapped with separator strips and twisted with positive electrodes. The above electrodes were encapsulated in a tube with injected electrolyte.

Fabrication of Power Supply System: The energy harvesting module consisted of 16 FGDSCs, in which eight FGDSCs were connected in series as a group and the two groups were connected in parallel. The energy-storing module consisted of eight fiber lithium-ion batteries connected in parallel. The conducive Cu wires were used as the electrical connections for these two modules.

Characterization: *J–V* curves of FGDSCs were measured with a source meter (Keithley 2420) from 0.9 to −0.2 V with a dwell time of 50 ms under simulated AM 1.5G sunlight. The FGDSCs were placed on a black plate, and covered with black masks at both sides. Multiple tests can be conducted by rotating fiber solar cells in situ, beneficial to characterize the uniformities of their performances and determine the PCE dependency on incident light direction. Surface morphologies and micro-scale channel sizes were characterized by scanning electron microscopy (SEM, Zeiss, operated at 3 kV). The rheological properties were characterized with a rotational rheometer (Thermo Fisher HAAKE MARS III). The adhesion strengths were tested by a universal testing machine (Heng Yi, Shanghai). The cyclic voltammetry curves, electrochemical activity areas, and electrochemical impedance spectra were measured by an electrochemical workstation (CHI 660E, Shanghai Chenhua). The cyclic voltammetry curves were measured in the methoxypropionitrile solution containing 5 mM I^-, 0.5 mM I_2, 0.05 M $LiClO_4$, and 20 wt% poly(ethylene adipate) at a scan rate of 50 mV·s^{-1} by three-electrode system (as-prepared electrode, Pt, and Ag/AgCl as working, counter and reference electrode, respectively). The electrochemical activity areas were characterized by cyclic voltammetry in an aqueous solution composed of 20 mM $K_4Fe(CN)_6$ and 0.2 M KCl at a scan rate of 20 mV s^{-1} by the same three-electrode system.[56] The normalized active areas were obtained by dividing the electrochemical activity area by the surface area of the electrodes. The electrochemical impedance spectroscopy was measured from 100 kHz to 0.01 Hz with an AC amplitude of 10 mV in the as-prepared gel electrolyte. Incident photon-to-current conversion efficiency (IPCE) spectra were measured by an external quantum efficiency measurement system containing a power meter (2936-R, Newport) and a monochromator (Cornerstone 260–74125, Newport). The involved wearable smart bracelet was a common commercial product and operated in strict accordance with the product instructions. The human experiments conformed to the regulations of the Animal and Human Experimentation Committee of Fudan University. A healthy subject from Fudan University had provided written informed consent before participating in the study.

Calculation of PCEs of FGDSCs: According to the standard calculation method,[57–59] the effective area of fiber solar cells was represented by the projected area of the photoanode, calculated from its effective length and average diameter. The PCE of fiber solar cells was calculated by the following equations:

$$PCE = \frac{I_{SC} \times V_{OC} \times FF}{A \times P_{in}} \quad (1)$$

$$A = d \times l \quad (2)$$

where I_{SC} is the short-circuit current, P_{in} is the power density of incident light, A is the projected area of the photoanode, d is the average diameter of the photoanode, and l is the effective length of the photoanode.

Statistical Analysis: PCE values of FGDSCs for comparison were presented as the average of three measured FGDSCs. Each determined channel size was the average value of fifty channel sizes measured at different parts of a fiber counter electrode. The electrochemical activity areas were presented as the mean ± standard deviation of three measured counter electrodes.

Supporting Information

Supporting Information is available from the Wiley Online Library or from the author.

Acknowledgements

This work was supported by the MOST (2022YFA1203001, 2022YFA1203002), the NSFC (T2321003, 22335003, 52122310, 22075050, 22105045), and the STCSM (21511104900).

Conflict of Interest

The authors declare no conflict of interest.

Data Availability Statement

The data that support the findings of this study are available in the supplementary material of this article.

Keywords

aligned channels, carbon nanotube, dye-sensitized solar cell, fiber, gel electrolyte

Received: March 12, 2024
Revised: April 16, 2024
Published online: May 7, 2024

[1] Z. Zhu, Z. Lin, W. Zhai, X. Kang, J. Song, C. Lu, H. Jiang, P. Chen, X. Sun, B. Wang, Z. S. Wang, H. Peng, *Adv. Mater.* **2024**, *36*, 2304876.
[2] X. Shi, Y. Zuo, P. Zhai, J. Shen, Y. Yang, Z. Gao, M. Liao, J. Wu, J. Wang, X. Xu, Q. Tong, B. Zhang, B. Wang, X. Sun, L. Zhang, Q. Pei, D. Jin, P. Chen, H. Peng, *Nature* **2021**, *591*, 240.

[3] A. Libanori, G. R. Chen, X. Zhao, Y. H. Zhou, J. Chen, *Nat. Electron.* **2022**, *5*, 142.
[4] Z. Z. Zhao, C. Yan, Z. X. Liu, X. L. Fu, L. M. Peng, Y. F. Hu, Z. J. Zheng, *Adv. Mater.* **2016**, *28*, 10267.
[5] G. Wang, J. Zhang, C. Yang, Y. Wang, Y. Xing, M. A. Adil, Y. Yang, L. Tian, M. Su, W. Shang, K. Lu, Z. Shuai, Z. Wei, *Adv. Mater.* **2020**, *32*, 2005153.
[6] Y. B. Zhang, X. H. Xia, K. K. Ma, G. Xia, M. Q. Wu, Y. H. Cheung, H. Yu, B. S. Zou, X. W. Zhang, O. K. Farha, J. H. Xin, *Adv. Funct. Mater.* **2023**, *33*, 2301607.
[7] W. J. Xu, S. T. Wu, X. M. Li, M. C. Zou, L. S. Yang, Z. L. Zhang, J. Q. Wei, S. Hu, Y. H. Li, A. Y. Cao, *Adv. Energy Mater.* **2016**, *6*, 1600095.
[8] W. J. Ma, Y. Zhang, S. W. Pan, Y. H. Cheng, Z. Y. Shao, H. X. Xiang, G. Y. Chen, L. P. Zhu, W. Weng, H. Bai, M. F. Zhu, *Chem. Soc. Rev.* **2021**, *50*, 7009.
[9] W. J. Zhai, Z. F. Zhu, X. M. Sun, H. S. Peng, *Adv. Fiber Mater.* **2022**, *4*, 1293.
[10] Y. K. Zhang, S. W. Ng, X. Lu, Z. J. Zheng, *Chem. Rev.* **2020**, *120*, 2049.
[11] M. D. Ye, X. R. Wen, M. Y. Wang, J. Iocozzia, N. Zhang, C. J. Lin, Z. Q. Lin, *Mater. Today* **2015**, *18*, 155.
[12] J. Song, Y. Gu, Z. Lin, J. Liu, X. Kang, X. Gong, P. Liu, Y. Yang, H. Jiang, J. Wang, S. Cao, Z. Zhu, H. Peng, *Adv. Mater.* **2024**, *36*, 2312590.
[13] Z. Zhu, Z. Lin, Y. Gu, J. Song, X. Kang, H. Jiang, H. Peng, *Adv. Funct. Mater.* **2023**, *33*, 2306742.
[14] X. Kang, Z. Zhu, T. Zhao, W. Zhai, J. Xu, Z. Lin, K. Zeng, B. Wang, X. Sun, P. Chen, *Adv. Funct. Mater.* **2022**, *32*, 2207763.
[15] C. S. Huang, S. Yakunin, J. Avaro, X. Y. Kang, M. I. Bodnarchuk, M. Liebi, X. M. Sun, R. M. Rossi, M. V. Kovalenko, L. F. Boesel, *Adv. Energy Mater.* **2022**, *12*, 2200441.
[16] Z. T. Zhang, X. L. Chen, P. N. Chen, G. Z. Guan, L. B. Qiu, H. J. Lin, Z. B. Yang, W. Y. Bai, Y. F. Luo, H. S. Peng, *Adv. Mater.* **2014**, *26*, 466.
[17] M. Peng, D. C. Zou, *J. Mater. Chem. A* **2015**, *3*, 20435.
[18] J. Ren, X. M. Sun, P. N. Chen, Y. G. Wang, H. S. Peng, *Chin. Sci. Bull.* **2020**, *65*, 3150.
[19] H. Iftikhar, G. G. Sonai, S. G. Hashmi, A. F. Nogueira, P. D. Lund, *Materials* **2019**, *12*, 1998.
[20] A. Rafique, I. Ferreira, G. Abbas, A. C. Baptista, *Nano-Micro Lett.* **2023**, *15*, 40.
[21] D. Lv, Q. Q. Jiang, Y. Y. Shang, D. Y. Liu, *npj Flexible Electron.* **2022**, *6*, 38.
[22] H. Sun, Y. Zhang, J. Zhang, X. M. Sun, H. S. Peng, *Nat. Rev. Mater.* **2017**, *2*, 17023.
[23] X. J. Xu, S. L. Xie, Y. Zhang, H. S. Peng, *Angew. Chem., Int. Ed.* **2019**, *58*, 13643.
[24] K. K. Sonigara, H. K. Machhi, J. V. Vaghasiya, A. Gibaud, S. C. Tan, S. S. Soni, *Small* **2018**, *14*, 1800842.
[25] Y. Ma, X. Meng, K. Li, L. Zhang, Y. Du, X. Cai, J. Qiu, *ACS Catal.* **2023**, *13*, 1290.
[26] U. Mehmood, H. Asghar, F. Babar, M. Younas, *Sol. Energy* **2020**, *196*, 132.
[27] G. R. Li, X. P. Gao, *Adv. Mater.* **2020**, *32*, 1806478.
[28] H. Zou, X. Meng, X. Zhao, J. Qiu, *Adv. Mater.* **2023**, *35*, 2207262.
[29] X. M. Fu, L. M. Xu, J. X. Li, X. M. Sun, H. S. Peng, *Carbon* **2018**, *139*, 1063.
[30] H. Zhang, W. Q. Zhao, M. C. Zou, Y. S. Wang, Y. J. Chen, L. Xu, H. S. Wu, A. Y. Cao, *Adv. Energy Mater.* **2018**, *8*, 1800013.
[31] H. Peng, P. Chen, X. Zhou, J. Xu, X. Kang, Y. Xu, K. Zhang, H. Jiang, T. Zhao, *Acta Chim. Sinica* **2023**, *81*, 565.
[32] B.-C. Xiao, L.-Y. Lin, *J. Colloid Interface Sci.* **2020**, *571*, 126.
[33] H.-W. Pang, H.-F. Yu, Y.-J. Huang, C.-T. Li, K.-C. Ho, *J. Mater. Chem. A* **2018**, *6*, 14215.
[34] M. S. M. Misenan, A. S. A. Khiar, T. Eren, *Polym. Int.* **2022**, *71*, 751.
[35] C. L. Chen, H. S. Teng, Y. L. Lee, *Adv. Mater.* **2011**, *23*, 4199.
[36] J. Song, G. Li, K. Xi, B. Lei, X. Gao, R. V. Kumar, *J. Mater. Chem. A* **2014**, *2*, 10041.
[37] S. M. Zakeeruddin, M. Grätzel, *Adv. Funct. Mater.* **2009**, *19*, 2187.
[38] H. J. Snaith, L. Schmidt-Mende, *Adv. Mater.* **2007**, *19*, 3187.
[39] H. Li, Z. Yang, L. Qiu, X. Fang, H. Sun, P. Chen, S. Pan, H. Peng, *J. Mater. Chem. A* **2014**, *2*, 3841.
[40] H. Sun, H. Li, X. You, Z. Yang, J. Deng, L. Qiu, H. Peng, *J. Mater. Chem. A* **2014**, *2*, 345.
[41] H. Li, J. Guo, H. Sun, X. Fang, D. Wang, H. Peng, *ChemNanoMat* **2015**, *1*, 399.
[42] J. H. Kwon, J. S. Kim, *J. Appl. Polym. Sci.* **2016**, *133*, 43439.
[43] N. Zhang, J. Chen, Y. Huang, W. Guo, J. Yang, J. Du, X. Fan, C. Tao, *Adv. Mater.* **2015**, *28*, 263.
[44] Z. Gao, P. Liu, X. Fu, L. Xu, Y. Zuo, B. Zhang, X. Sun, H. Peng, *J. Mater. Chem. A* **2019**, *7*, 14447.
[45] J. H. Kim, S.-J. Koo, H. Cho, J. W. Choi, S. Y. Ryu, J.-W. Kang, S.-H. Jin, C. Ahn, M. Song, *ACS Sustainable Chem. Eng.* **2020**, *8*, 15065.
[46] J. H. Kim, S. K. Hong, S.-J. Yoo, C. Y. Woo, J. W. Choi, D. Lee, J.-W. Kang, H. W. Lee, M. Song, *Dyes Pigm.* **2021**, *185*, 108855.
[47] J. H. Kim, D. S. Utomo, D. Lee, J. W. Choi, M. Song, *J. Power Sources* **2021**, *512*, 230496.
[48] J. H. Kim, S.-J. Yoo, D. Lee, J. W. Choi, S.-C. Han, T. I. Ryu, H. W. Lee, M. Shin, M. Song, *Nano Res.* **2021**, *14*, 2728.
[49] D. S. Utomo, J. H. Kim, D. Lee, J. Park, Y.-C. Kang, Y. H. Kim, J. W. Choi, M. Song, *J. Colloid Interface Sci.* **2021**, *584*, 520.
[50] P. An, J. H. Kim, M. Shin, S. Kim, S. Cho, C. Park, G. Kim, H. W. Lee, J. W. Choi, C. Ahn, M. Song, *Nanomaterials* **2022**, *12*, 2309.
[51] J. H. Kim, H. W Park, S.-J. Koo, D. Lee, E. Cho, Y.-K. Kim, M. Shin, J. W Choi, H. J Lee, M. Song, *J. Energy Chem.* **2022**, *67*, 458.
[52] J. H. Kim, S.-J. Koo, J. Y. Cheon, Y. Jung, S. Cho, D. Lee, J. W. Choi, T. Kim, M. Song, *Nano Energy* **2022**, *96*, 107054.
[53] J. H. Kim, E. Cho, G.-g. Kim, C. Park, S. Kim, S. Y. Ryu, J. W. Choi, H. J. Lee, M. Song, *Dyes Pigm.* **2023**, *219*, 111575.
[54] J. H. Kim, D. S. Utomo, D. Lee, S. Cho, M. Song, J. W. Choi, *J. Mater. Chem. C* **2023**, *11*, 11980.
[55] Y. Rong, Y. Hu, S. Ravishankar, H. Liu, X. Hou, Y. Sheng, A. Mei, Q. Wang, D. Li, M. Xu, *Energy Environ. Sci.* **2017**, *10*, 2383.
[56] S. Hrapovic, Y. L. Liu, K. B. Male, J. H. T. Luong, *Anal. Chem.* **2004**, *76*, 1083.
[57] Y. P. Fu, H. W. Wu, S. Y. Ye, X. Cai, X. Yu, S. C. Hou, H. Kafafy, D. C. Zou, *Energy Environ. Sci.* **2013**, *6*, 805.
[58] M. R. Lee, R. D. Eckert, K. Forberich, G. Dennler, C. J. Brabec, R. A. Gaudiana, *Science* **2009**, *324*, 232.
[59] Y. P. Fu, Z. B. Lv, S. C. Hou, H. W. Wu, D. Wang, C. Zhang, Z. Z. Chu, X. Cai, X. Fan, Z. L. Wang, D. C. Zou, *Energy Environ. Sci.* **2011**, *4*, 3379.

